nature communications

Article

https://doi.org/10.1038/s41467-026-70506-z

Single-cell and spatial profiling reveal cDC2A-CXCL13^{+}CD8^{+} T-epithelial cell crosstalk and cytotoxicity through TNFRSF9 in cutaneous and mucosal lichen planus

Received: 30 June 2025

Accepted: 26 February 2026

Published online: 14 March 2026

Check for updates

Rundong Jiang[1,2], Rachael Bogle[1], Xianying Xing[1], Joseph Kirma[1], Jennifer Fox[1], Paul W. Harms[1,3], Tran Do[1], Allison C. Billi[1], J. Michelle Kahlenberg[4], Robert L. Modlin[5], Rosane Teles[5], Julie West[5], Aaron Mangold[6], Haihan Zhang[7], Martin A. Schneider[8], Sandro Bruno[8], Ben Roediger[8], Georg Martiny-Baron[8], Lam C. Tsoi[1], Feriel Hacini-Rachinel[8], Till A. Röhn[8] & Johann E. Gudjonsson[1,2,4]

Lichen planus (LP) is a chronic inflammatory disease of the skin and mucous membranes, marked by T cell infiltration and keratinocyte apoptosis. However, its immune microenvironment remains poorly understood. Using single-cell RNA sequencing, spatial transcriptomics, and proteomics on samples from 28 patients and 18 healthy controls, we identify elevated interferon (IFN) and cytotoxic signatures in CXCL13^{+}CD8^{+} T cells in both cutaneous and mucosal LP, but not in lichen planopilaris. T cells expressing TNF and IFNG are spatially linked to epithelial cells through ligand-receptor interactions, correlating with inflammation. We identify cDC2A cells as key contributors, proximal to CXCL13^{+}CD8^{+} T cells, serving as a major source of IL-15. CXCL13^{+}CD8^{+} T cells express TNFRSF9 (4-1BB), which enhances their cytotoxic responses in the skin. In summary, our data reveal a critical role for cDC2A in driving CXCL13^{+}CD8^{+} T–epithelial cytotoxicity in cutaneous and mucosal LP through TNFRSF9.

Lichen planus (LP) is a chronic, T cell-mediated inflammatory disease with unclear etiology, affecting approximately 2% of the global population with marked impact on quality of life[1]. LP is characterized by widespread pruritic skin lesions, with frequent involvement of painful oral and genital mucosal erosions and nail changes[1]. Several clinical subtypes of LP have been described based on lesion morphology and anatomical distribution, including cutaneous lichen planus (CLP), mucosal lichen planus (MLP), and lichen planopilaris (LPP) primarily involving hair follicles including on the scalp[2–4]. Histologically, LP is characterized by a dense band-like infiltration of lymphocytes, especially cytotoxic CD8^{+} T cells[5,6], localized along the dermal-epidermal junction, accompanied by basal keratinocyte apoptosis[7].

The current understanding of LP pathogenesis is largely based on immunohistochemistry and bulk transcriptomic analyses[8] focusing on a limited number of cellular contributors, such as keratinocytes and CD8^{+} T cells[5]. To date, LP has been characterized as an interferon (IFN)-

[1]Department of Dermatology, University of Michigan, Ann Arbor, MI, USA. [2]Graduate Program in Immunology, University of Michigan, Ann Arbor, MI, USA. [3]Department of Pathology, University of Michigan, Ann Arbor, MI, USA. [4]Department of Internal Medicine, Division of Rheumatology, University of Michigan, Ann Arbor, MI, USA. [5]Department of Dermatology, University of California Los Angeles (UCLA), Los Angeles, CA, USA. [6]Department of Dermatology, Mayo Clinic, Scottsdale, AZ, USA. [7]Department of Biostatistics, University of Michigan, Ann Arbor, MI, USA. [8]Immunology Disease Area, Novartis BioMedical Research, Novartis Pharma AG, Basel, Switzerland. e-mail: johanng@med.umich.edu

γ driven inflammatory disorder, marked by $CD8^+$ T cell mediated cytotoxicity directed against keratinocytes[7,9], with some studies having proposed a role for IL-17[10,11]. However, the potential pathogenic contributions of other cell populations and cytokines have received comparative limited attention. Our team previously identified a unique $CXCL13^+CD8^+$ cytotoxic T cell population in CLP skin[12], suggesting that the immune complexity of LP is broader than previously appreciated. Moreover, the immune microenvironment and molecular dysregulation underlying the various clinical subtypes of LP remain poorly understood—particularly regarding the common and divergent pathogenic mechanisms across subtypes. A deeper understanding of these mechanisms is crucial for developing targeted therapies and addressing the challenges of treating LP and its diverse clinical forms.

Here, we present a comprehensive molecular characterization of LP by integrating single-cell RNA sequencing, spatial transcriptomics, and spatial proteomics across 45 skin samples derived from CLP, LPP, MLP, and healthy controls. Building upon our previous identification of $CXCL13^+CD8^+$ cytotoxic T cells in CLP skin, we further delineate their developmental trajectory, highlighting the role of IL-15 signaling released from neighboring cDC2A cells in driving their effector function. Moreover, through spatial proteomic analysis and our previously established keratinocyte-PBMC coculture model, we identify *TNFRSF9* (4-1BB) as a key effector molecule and a potential therapeutic target for CLP.

Results

scRNA-seq reveals cellular diversity across different clinical subtypes of LP lesions

To comprehensively interrogate the unbiased cellular composition and immune microenvironment of LP at single-cell resolution, we performed single-cell RNA sequencing (scRNA-seq) on cutaneous specimens from 16 CLP patients (including one patient with both CLP and MLP, for whom the biopsy was obtained from skin tissue [CLP]), along with 9 healthy control skin samples. In addition, our dataset included scalp biopsies from 6 LPP patients and 5 matched healthy scalp controls, as well as oral mucosal biopsies from 6 MLP patients and 4 healthy mucosal controls (Fig. 1A). After stringent quality control, a total of 223,806 cells were retained for downstream analysis and

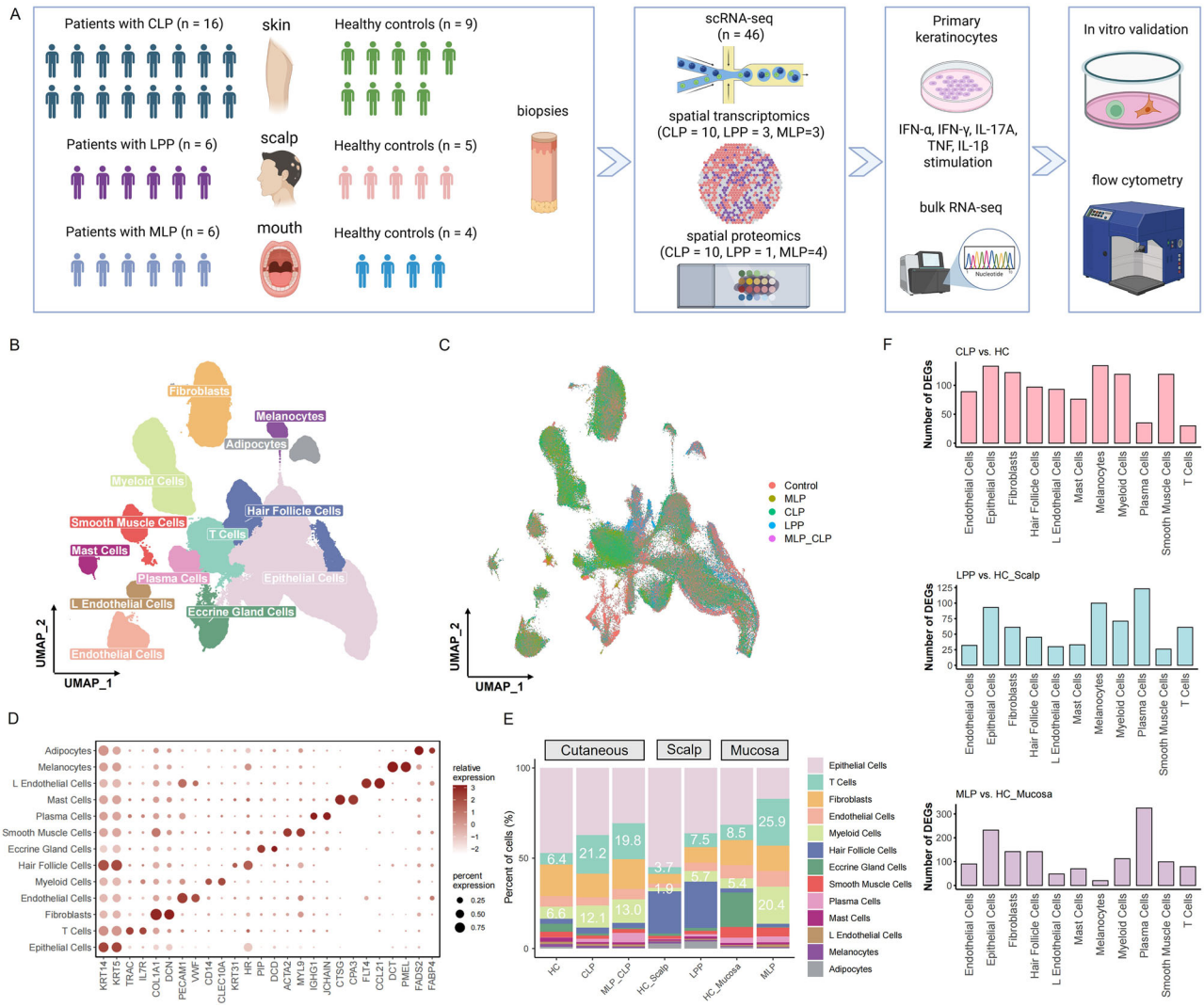

Fig. 1 | scRNA-seq reveals cellular diversity across different clinical subtypes of LP. A Workflow of the research design. Created in BioRender. Jiang, R. (2026) https://BioRender.com/tz1wzoh. **B** UMAP plot of 223,806 cells colored by cell types. **C** UMAP plot showing cells colored by disease conditions. **D** Dot plot showing representative marker genes for each cell type. The color scale represents the scaled expression average of each gene. **E** Bar charts showing proportion of main cell types in different groups. **F** Number of DEGs per cell type for CLP (up), LPP (middle) and MLP (down). (adjusted *P* value < 0.05, absolute $\log_2$FC > 1). *P* value was calculated by two-sided Wilcoxon test with Bonferroni correction. CLP cutaneous lichen planus, LPP lichen planopilaris, MLP mucosal lichen planus, MLP_CLP patients diagnosed with both MLP and CLP, with biopsy samples collected from CLP lesions.

https://doi.org/10.1038/s41467-026-70506-z

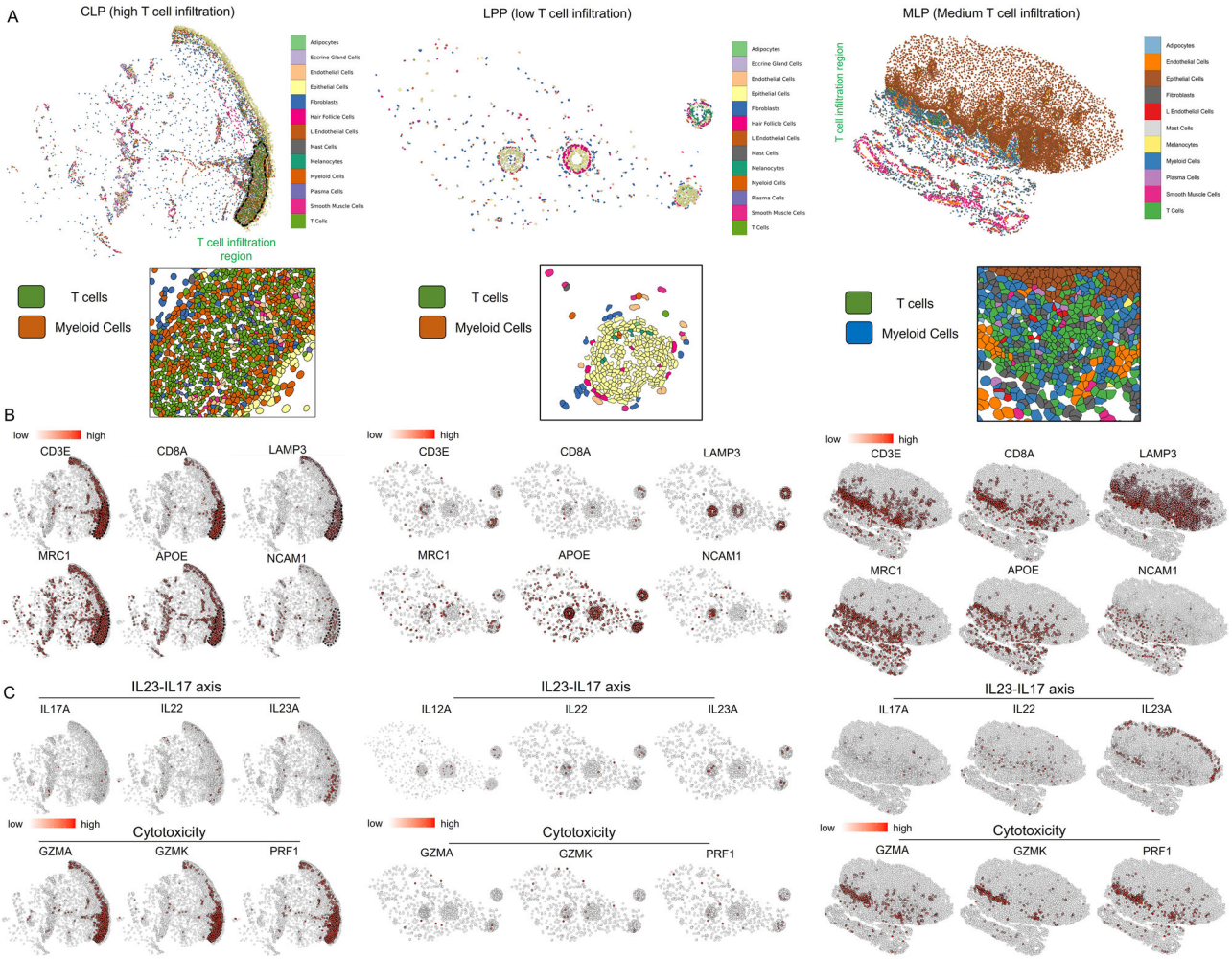

Fig. 2 | Spatial transcriptomics identifies cytotoxic activity and abundant infiltration of CD8⁺ T cells. A Annotated spatial map of CLP, LPP, and MLP lesions. Black dashed lines denote T cell infiltration region in CLP. White dashed lines denote T cell infiltration region in MLP. Representative images of single cell segmentation of each group are listed below. **B** Spatial expression levels of selected marker genes of main cell type. **C** Spatial expression levels of selected marker genes from the IL-23-IL-17 axis and cytotoxic response.

categorized into 13 major cell populations: Epithelial cells (*KRT5*, *KRT14*), T cells (*TRAC*, *IL7R*), Fibroblasts (*COL1A1*, *DCN*), Endothelial cells (*PECAM1*, *VWF*), Myeloid cells (*CD14*, *CLEC10A*), Hair follicle cells (*KRT31*, *HR*), Eccrine gland cells (*PIP*, *DCN*), Smooth muscle cells (*ACTA2*, *MYL9*), Plasma cells (*IGHG1*, *JCHAIN*), Mast cells (*CTSG*, *CPA3*), Lymphatic endothelial cells (*CCL21*, *FLT4*), Melanocytes (*DCT*, *PMEL*), and Adipocytes (*FADS2*, *FABP4*) (Fig. 1B, D and Supplementary Fig. 1A, B). Each cell population included cells from control, CLP, LPP, MLP, and MLP_CLP (patients diagnosed with both CLP and MLP) samples (Fig. 1C). Notably, two kinds of immune cell populations, T cells and Myeloid cells, were significantly enriched in LP lesions, especially in CLP and LPP, compared to healthy controls (Fig. 1E and Supplementary Fig. 1C), suggesting a marked accumulation of immune infiltrates and heightened local immune activation. To discern heterogeneity in different cell composition between healthy control and affected skin lesions, we first calculated the differentially expressed genes (DEGs) between (i) CLP and HC skin, (ii) LPP and HC scalp, and (iii) MLP and HC mucosa. In each comparison, we required absolute $\log_2$ fold-change > 1 ($|\log_2 FC| > 1$) and adjusted $P < 0.05$ of genes for further consideration (Fig. 1F). Impressively, epithelial cells exhibited a consistently high number of DEGs distinguishing inflamed lesions from healthy skin across all three clinical subtypes of LP, in line with the known immune responses against keratinocytes[7,8]. In contrast, notable heterogeneity among plasma cells was observed specifically in LPP and MLP lesions.

Spatial transcriptomics identify pronounced cytotoxic activity and abundant infiltration of CD8⁺ T cells

To spatially localize the major cell types identified by scRNA-seq within LP lesions, we performed spatial transcriptomic profiling (spatial-seq) using the Xenium platform on ten independent CLP skin samples, three LPP scalp samples, and three MLP oral mucosa samples. We deconvoluted the spatial boundaries by the major cell types detected in scRNA-seq using Giotto function (Methods) and validated the accuracy of these deconvolution results (Supplementary Fig. 1D-G). The epidermal architecture and dense, band-like infiltration of T cells and myeloid cells along the epithelial layers were clearly visualized, particularly in CLP lesions, whereas MLP lesions displayed a more limited infiltration area, with moderate T cell and myeloid cell infiltration (Fig. 2A and Supplementary Fig. 2A-D). In sharp contrast, immune cell infiltration was markedly less prominent in LPP lesions (Fig. 2A, middle), in agreement with the cellular composition inferred from scRNA-seq analysis (Fig. 1E). These localization results underscored the high spatial resolution and quality of our dataset. The immune cell infiltration regions were distinguished by high expression of *CD3E*, *CD8A*, *LAMP3* (a marker of cDC2A), and *MRC1* in CLP and MLP lesions. By contrast, this co-expression was not observed in the LPP lesions (Fig. 2B), further highlighting the reduced immune activation in this subtype. Of note, the inflammatory mechanisms underlying LP pathogenesis remain a subject of debate. While previous studies have

implicated IL-17 signaling in LP[10], our spatial transcriptomic analysis provided compelling evidence for a dominant cytotoxic response within LP lesions, characterized by elevated expression of *GZMA*, *GZMK*, and *PRF1* in the T cell infiltration region, and mostly an absence of IL-23/IL-17 driven inflammatory signature (Fig. 2C). The lack of IL-23/IL-17 signaling activation in LP lesions was further confirmed by immunofluorescent staining (Supplementary Fig. 2E). These findings suggest that cytotoxic T cell mediated tissue injury, rather than Th17 mediated inflammation, may play a more central role in LP pathology, particularly in CLP and MLP.

scRNA-seq defines cDC2A and LAM as activated myeloid subsets in LP

To examine cellular heterogeneity in myeloid cells in LP skin, we subclustered myeloid cells and annotated ten myeloid subpopulations: plasmacytoid DC (pDC; *JCHAIN*, *IGKC*), Langerhans cells (LC; *CD1A*, *CD207*), classical type 1 dendritic cells (cDC1; *XCR1*, *CLEC9A*), classical type 2 dendritic cells subset A (cDC2A; *LAMP3*, *CCR7*), classical type 2 dendritic cell subset B (cDC2B; *CD1C*, *CLEC10A*), MRC1$^+$ Macrophage (MRC1+ Mac; *MRC1*, *CD209*), lipid-associated macrophage (LAM; *APOE*, *CTSD*), perivascular macrophage (PVM; *SELENOP*, *F13A1*), IRF7$^+$ cells (IRF7+; *IRF7*, *S100A9*), and cycling cells (Cycling; *TOP2A*, *MKI67*) (Fig. 3A, B). Analysis of cellular composition across disease groups revealed a consistently increased proportion of cDC2A and LAM cells in all three LP subtypes (Fig. 3C). These findings were consistent with our spatial-seq analysis, which showed ubiquitous expression of *LAMP3* and *APOE* (marker of LAM cells), beneath the epithelial layer in CLP and MLP, and surrounding hair follicles in LPP (Fig. 2B). Moreover, both scRNA-seq and spatial transcriptomics revealed widespread infiltration of MRC1$^+$ macrophages in CLP and MLP lesions, whereas such infiltration was minimal in LPP lesions (Fig. 2B and Fig. 3C). Notably, among all myeloid cell subsets, cDC2A and LAM cells exhibited the highest levels of inflammatory response and IFN-γ response activity (Fig. 3D), highlighting their potential central role in driving LP-associated inflammation. We next identified upregulated genes in each LP subtype by comparing them to their matched healthy controls. CLP and MLP lesions exhibited the most abundant DEGs in both cDC2A and LAM cells, whereas LPP lesions showed transcriptional heterogeneity primarily within LAM cells (Fig. 3E). In addition, analysis of the upregulated pathway of the cDC2A in CLP revealed their extensive involvement in Toll-like receptor signaling pathway and TNF signaling pathway (Fig. 3F). In line with our previous findings in psoriasis[13], cDC2A expressed high levels of the co-stimulatory molecules *CD40*, *CD80*, and *CD83* (Supplementary Fig. 3A), suggesting that these cells may drive T cell activity and expansion in LP lesions. Strikingly, cDC2A cells from CLP and MLP lesions exhibited upregulation of multiple co-stimulatory molecules, including *CD40*, *CD80*, *CD83*, *CD200*, and *CD274*, as well as key inflammatory mediators such as *LYZ* (lysozyme), *IL12B*, *CXCL9*, *CXCL10*, and *CCL19* (Fig. 3G). In addition, we also found a relative increase in the expression of interferon regulatory factors (*IRF1*, *IRF8*) and the NF-κB component *NFKB1* in these LP subtypes (Fig. 3G). These findings suggest that cDC2A cells may play a more prominent role in the pathogenesis of CLP and MLP, while their involvement in LPP appears limited.

We next examined the potential role of LAM cells in the pathogenesis of LP. While the increase in LAM cell infiltration in LPP compared with healthy scalps did not reach statistical significance (Supplementary Fig. 3C), pathway enrichment analysis of upregulated genes in LAM cells revealed strong associations with the lysosome pathway and leukocyte transendothelial migration, particularly in LPP (Supplementary Fig. 3B). In contrast, the enriched pathways identified in the CLP and MLP groups were less pronounced and lacked clear functional relevance. Notably, lysosome-related genes such as *CSTB*, *CTSK*, and *LYZ*, as well as co-stimulatory molecules *CD84* and *CD276*, were markedly upregulated in LPP lesions (Supplementary Fig. 3D). These findings suggest that LAM cells in LPP may contribute to disease pathogenesis through enhanced antigen processing and presentation.

T cells infiltrating LP lesions demonstrate cytotoxic effect in both CLP and MLP

LP shows prominent T cell infiltration (Fig. 2A), but the nature of the T cell involvement has not previously been addressed. Here, we identified 6 subclusters of T cells in LP, including IFN T cells (*IFI44L*, *IFI6*, *STAT1*), Treg (*FOXP3*, *CTLA4*, *IL2RA*), NK (*KLRD1*, *KLRC3*, *NCAM1*, *NKG7*, *GNLY*), CXCL13$^+$CD8 (*CXCL13*, *IFNG*, *GZMB*, *CD8A*), GZMK$^+$CD8 (*GZMK*, *GZMA*, *CCL5*, *CD8A*), Tem (*RGCC*, *LMNA*, *FOSB*), and Tcm (*IL7R*, *TCF7*, *CD40LG*) (Fig. 4A, B). Consistent with our previous clinical study in LP patients[12], we consistently identified a population of CXCL13$^+$CD8$^+$ cells in the current scRNA-seq dataset. To further characterize these cells, we performed enrichment analysis on their top 50 marker genes, revealing strong associations with viral infection pathways and T cell differentiation programs (Fig. 4C). Intriguingly, our dataset also identified another CD8$^+$ T cell subset, referred to as GZMK$^+$CD8$^+$ cells, which are characterized by high expression of granzyme K (*GZMK*) and low expression of granzyme B (*GZMB*), a feature similarly observed in rheumatoid arthritis[14]. In line with previous findings[14], compared to CXCL13$^+$CD8$^+$ cells, GZMK$^+$CD8$^+$ cells in lesions exhibited relatively lower expression levels of key cytotoxicity-associated genes, including *IFNG* and *GZMB*, while displaying relatively higher expression of early activation markers, such as *GZMA* and *GZMK* (Fig. 4B)[15], suggesting an early differentiation state in this cluster. Given the well-established involvement of IFN signaling in LP pathogenesis, we also uncovered a distinct subset of IFN-responsive T cells, marked by robust expression of IFN-stimulated genes (Fig. 4B). Notably, these IFN T cells exhibited the highest enrichment for the IFN-γ response pathway (Fig. 4D).

Given distinct clinical and histopathological features in these three LP subtypes, we examined differences in T cell subtype composition among three subtypes (Supplementary Fig. 4A). Compared with healthy controls, CLP lesions exhibited a specific expansion of NK cells (Fig. 4E), while the IFN T cell population was relatively enriched in MLP (Fig. 4E). Similarly, CXCL13$^+$CD8$^+$ cells were also abundant in inflammation in both CLP and MLP but more pronounced in CLP based on the average cell proportions (Fig. 4E). As expected, cytotoxic effector genes, including *GZMB*, *PRF1*, and *IFNG*, were predominantly expressed in NK and CD8$^+$ T (CXCL13$^+$CD8$^+$) cells from CLP lesions, as well as in IFN T cells and CD8$^+$ T cells from MLP lesions. In contrast, LPP lesions exhibited minimal cytotoxic activity (Fig. 4F).

Furthermore, differential expression analysis (CLP vs. HC and MLP vs. HC_Mucosa) revealed that Tem and NK cells exhibited the most prominent transcriptional responses in CLP lesions, whereas NK cells and IFN T cells showed the strongest gene expression changes in MLP lesions (Supplementary Fig. 4B). In stark contrast, only a limited number of DEGs were identified in LPP lesions compared to healthy scalp controls (Supplementary Fig. 4B). Of note, due to the scarcity of CXCL13$^+$CD8$^+$ T cells in healthy samples, we were unable to fully evaluate the potential heterogeneity within this population. Strikingly, a consistent set of upregulated genes—including type I IFN downstream targets such as *IFI6*, *IFI27*, *IFI44L*, *MX1*, and *STAT1*—was observed in both CLP and MLP lesions across these T cell populations (Supplementary Fig. 4C), compared with healthy skin and mucosa, suggesting a highly IFN-stimulated microenvironment in LP lesions. Intriguingly, unlike other type I inflammation-related skin diseases such as vitiligo[16,17], classical tissue-resident memory T cell markers, including *ITGA1* (CD49a), *CD69*, and *CXCR6*, were not significantly expressed in our T cell populations (Supplementary Fig. 4D), suggesting limited involvement of tissue-resident memory T cells in LP pathogenesis.

Epithelial cells from the lesional skin of patients with LP exhibit a pathologic IFN signature

Given the well-established histological feature of keratinocyte apoptosis in LP lesions[7], we sought to delineate shared pathological processes across different LP subtypes. To this end, we subclustered epithelial cells and annotated their subtypes based on differentiation

https://doi.org/10.1038/s41467-026-70506-z

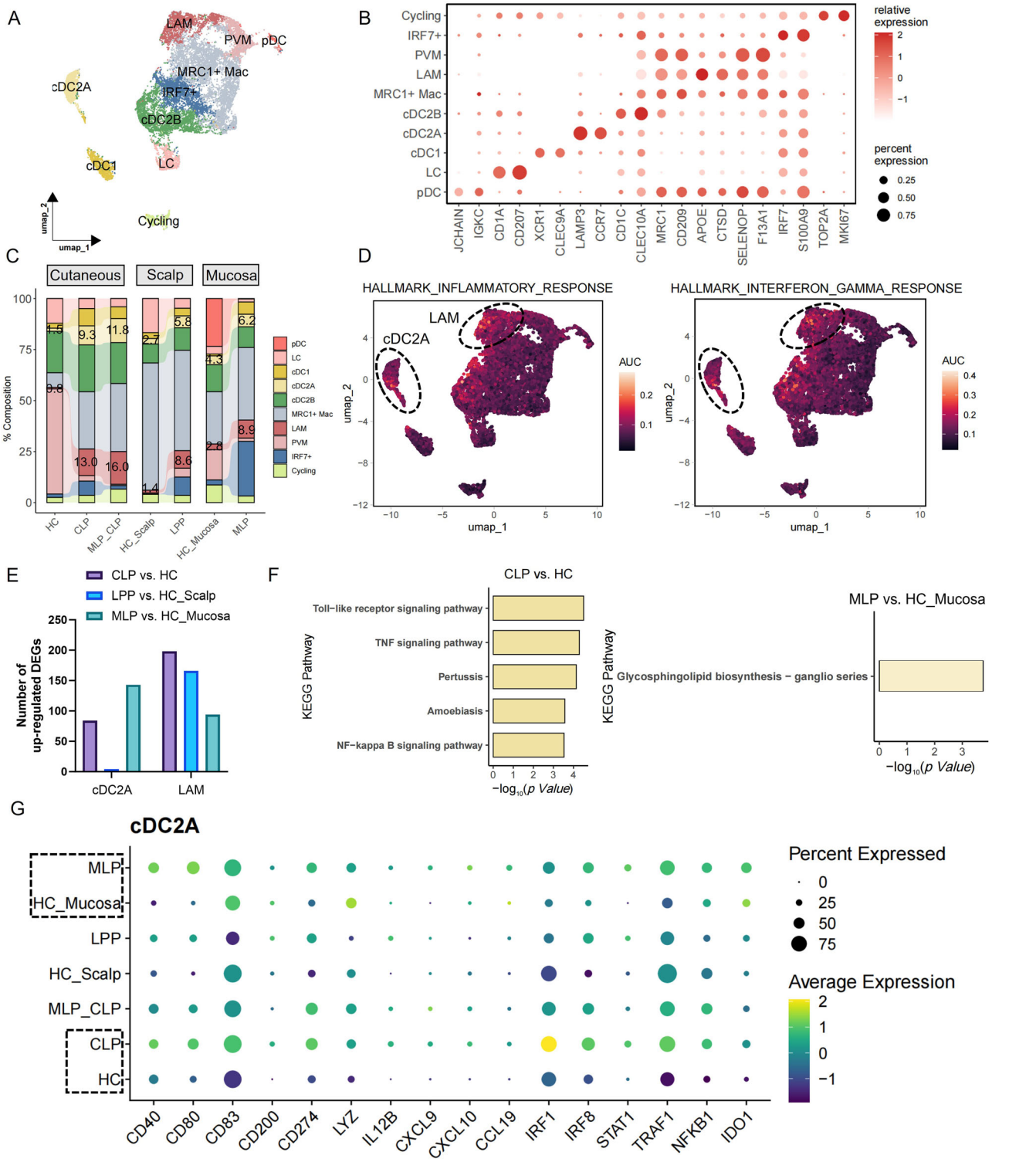

Fig. 3 | scRNA-seq defines cDC2A and LAM as activated myeloid subsets in LP. **A** UMAP plot showing myeloid cells colored by subtypes. **B** Dot plot showing the representative marker genes for each subtype. **C** Bar charts showing proportion of myeloid subtype in different groups. **D** UMAP plot showing individual cell AUC score for INFLAMMATORY_RESPONSE and INTERFERON_GAMMA_REPONSE activity in myeloid cells. **E** Number of DEGs (adjusted *P* value < 0.05, $\log_2$FC > 2; on *y* axis) for cDC2A and LAM population for CLP (left), LPP (middle) and MLP (right). *P* value was calculated by two-sided Wilcoxon test with Bonferroni correction. **F** KEGG pathway analysis of upregulated genes in cDC2A cells from CLP versus control skin, and MLP versus healthy mucosa. KEGG pathway enrichment was performed using a hypergeometric test, and *P* values were adjusted for multiple testing using the Benjamini–Hochberg method. **G** Dot plots of selected marker genes for each sample group.

https://doi.org/10.1038/s41467-026-70506-z

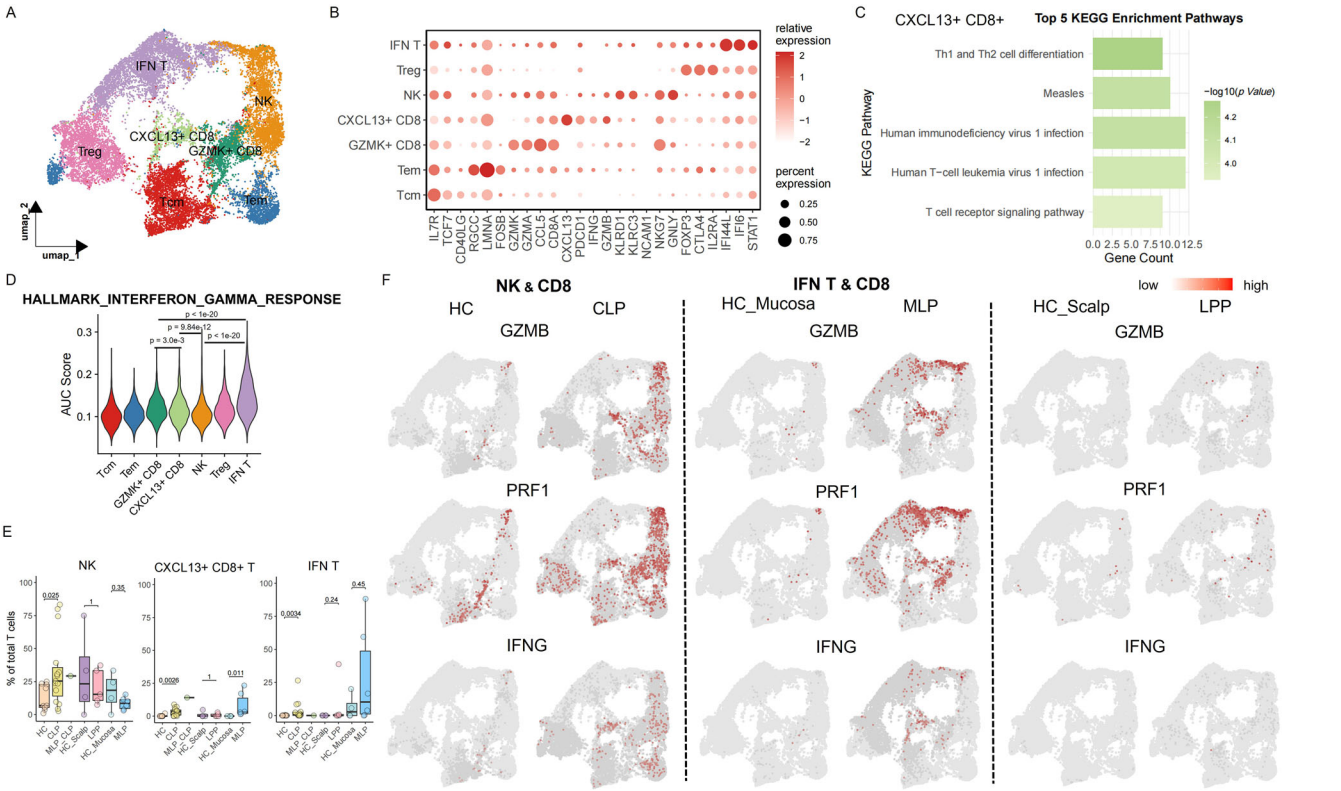

Fig. 4 | T cells infiltrating LP lesions demonstrate cytotoxic effect in both CLP and MLP. A UMAP plot showing T cells colored by subtypes. **B** Dot plot showing the representative marker genes for each subtype. **C** KEGG pathway analysis of the CXCL13$^+$CD8$^+$ cells. KEGG pathway enrichment was performed using a hypergeometric test, and *P* values were adjusted for multiple testing using the Benjamini–Hochberg method. **D** Violin plot showing the pathway enrichment scores of INTERFERON_GAMMA_REPONSE among T cell subtypes. The *P* values were calculated by two-sided Wilcoxon test. **E** Boxplots showing proportion of different subtype (NK, CXCL13$^+$CD8$^+$, IFN T cells) out of total T cells. HC ($n = 9$), CLP ($n = 15$), MLP_CLP ($n = 1$), HC_Scalp ($n = 4$), LPP ($n = 5$), HC_Mucosa ($n = 4$), and MLP ($n = 6$). Box plots show the median (center line), interquartile range (box), and 1.5× interquartile range (whiskers). The *P* values were calculated by two-sided Wilcoxon test. **F** UMAP plots showing the expression level of *GZMB*, *PRF1*, and *IFNG* in different LP groups. Source data are provided as a Source Data file.

states. Our analysis defined four distinct differentiation states, including Cycling (*TOP2A*, *MKI67*, *CDK1*), Basal (*KRT5*, *KRT14*, *COL17A1*), Differentiated (*THBD*, *KRT1*, *KRT10*), and Terminally differentiated (*LOR*, *FLG*, *LCN2*) keratinocytes (Fig. 5A, B). All clinical conditions were broadly represented across differentiation states (Supplementary Fig. 5A). We next identified multiple genes significantly upregulated in LP subtypes compared to their matched healthy controls ($\log_2$ fold change >1, adj. $p < 0.05$). We observed the elevated expression of IFN-associated downstream genes, including *CXCL9*, *CXCL10*, *CXCL11*, and *IFI44L* in several differentiated states of CLP epithelial cells (Fig. 5C), indicating a prominent IFN-enriched environment. These findings were further validated by immunofluorescent staining, which confirmed the predominant presence of CXCL9 + KRT5+ keratinocytes in CLP lesions (Fig. 5D). Additionally, MLP epithelial cells exhibited increased expression of *IL24*, a member of the IL-10 cytokine family, as well as the lymphocyte-associated mediator *CXCL13* and *IL23A* (Fig. 5C). To corroborate the key upstream regulators, we calculated module scores using genes induced in cultured keratinocytes stimulated by individual proinflammatory cytokines, including type I IFN (IFN-α), type II IFN (IFN-γ), IL-17A, TNF, and IL-1β. Consistent with the DEGs analysis, both IFN-α and IFN-γ signaling scores progressively increased from healthy skin to CLP lesions across Cycling, Basal, and Differentiated keratinocyte layers, as well as from healthy mucosa to MLP Cycling cells. In contrast, other cytokine signaling pathways remained comparable between LP lesions and healthy controls (Fig. 5E). Furthermore, in line with the cytokine signal scoring, the Area Under the Curve (AUC) scores of "Interferon alpha response", "Interferon gamma response", and "Inflammation response" pathways were consistently increased in CLP and MLP lesions, compared to healthy controls (Supplementary Fig. 5B). These results indicate a prominently IFN-activated epithelial inflammatory microenvironment in CLP and MLP.

To trace the source of these IFN signals, we performed receptor-ligand interaction analysis between epithelial cells and various T cell subtypes across all three LP clinical subtypes by using NicheNet[18]. Differential cell-cell interaction analyses revealed CLP- and MLP-specific *IFNG* signaling originating from CXCL13$^+$CD8$^+$ T cells targeting epithelial cells (Fig. 5F). This finding was further supported by spatial transcriptomics and immunofluorescence, which revealed a dense, band-like infiltration of CXCL13$^+$CD8$^+$ cells within the epithelial layer of both CLP and MLP lesions (Fig. 5, G and H). In stark contrast, LPP lesions exhibited minimal IFN-associated intercellular signaling, engaging neither epithelial cells (Fig. 5F) nor hair follicle cells (Supplementary Fig. 6A).

Cellular communication analysis reveals cDC2A cells-CXCL13$^+$CD8$^+$ T cells communication through IL-15 signaling

Given the prominent role of CXCL13$^+$CD8$^+$ cells in LP-associated inflammation, we next investigated potential ligand–receptor interactions originating from myeloid cells that may contribute to their activation and maintenance through CellChat[19]. In CLP lesions, both GZMK$^+$CD8$^+$ cells and CXCL13$^+$CD8$^+$ cells received IL-15 signaling, with a higher interaction probability observed in CXCL13$^+$CD8$^+$ cells, predominantly derived from cDC2A populations (Fig. 6A). Consistently, *IL15* expression was primarily restricted to cDC2A cells among all myeloid cells (Fig. 6B). Notably, although IL-7 signaling was

https://doi.org/10.1038/s41467-026-70506-z

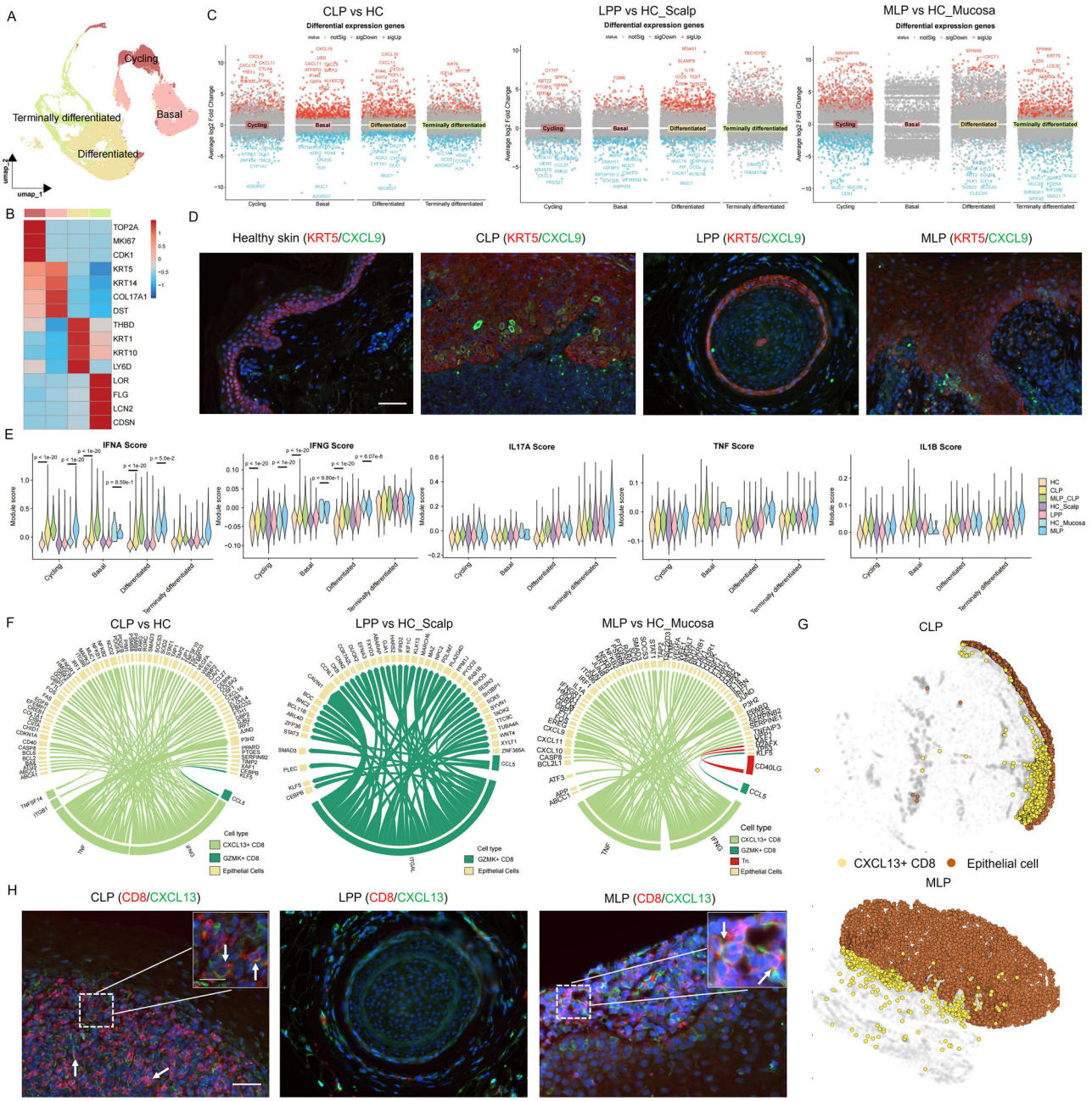

Fig. 5 | Epithelial cells from lesional skin of patients with LP exhibit a pathologic IFN signature. A UMAP plot showing keratinocytes colored by subtypes. **B** Heatmap showing the representative marker genes for each subtype. **C** Dot plot showing differentially expressed genes across keratinocyte subtypes in CLP versus control skin (left), LPP versus healthy scalp (middle), and MLP versus healthy mucosa (right). Red dot indicates genes upregulated in LP lesions, and blue dot indicates genes upregulated in healthy controls. **D** Immunofluorescence showing the colocalization of CXCL9 with KRT5 in the epithelial tissue of LP lesions and healthy control. Images shown are representative of $N = 3$. Scale bar = 100 μm. **E** Violin plots of KC scores for the indicated cytokine modules split by disease groups. The *P* values were calculated by two-sided Wilcoxon test. **F** Circos plots showing ligand–receptor interactions with higher interaction scores in CLP versus control skin (left), LPP versus healthy scalp (middle), and MLP versus healthy mucosa (right). Ligands are expressed by T cells, and receptors are expressed by epithelial cells. **G** Representative images of spatial distribution of $CXCL13^{+}CD8^{+}$ cells and epithelial cells in CLP (up) and MLP (bottom) lesions. **H** Immunofluorescence showing the colocalization of CXCL13 with CD8 in LP lesions. The white arrow points to the region of colocalization. Images shown are representative of $N = 3$. Scale bar = 100 μm; Scale bar = 50 μm in amplified image.

detected in the CellChat analysis (Fig. 6A), *IL7* expression was barely observed across myeloid subtypes (Supplementary Fig. 3E). Given the established role of the IL-7 signaling axis in TRM17 cell commitment[20], we speculate that IL-15, rather than IL-7, may play a more pivotal role in LP pathogenesis. To further corroborate the myeloid source of *IL15*, we examined co-expression of *IL15* with *IL12B* and found both cytokines to be abundantly expressed by cDC2A cells, specifically in CLP lesions (Fig. 6C). As expected, we then observed a marked expansion of cDC2A cells in CLP and MLP lesions, whereas such enrichment was not evident in LPP (Fig. 6D). Notably, despite the relatively low *IL15* expression observed in MLP lesions, a stronger interaction signal was still detected in $CD8^{+}$ cells, compared with healthy controls (Fig. 6E). Moreover, spatial transcriptomics revealed prominent spatial proximity between $CXCL13^{+}CD8^{+}$ cells and cDC2A cells in CLP lesions, with a comparatively reduced co-localization pattern observed in MLP lesions (Fig. 6H).

https://doi.org/10.1038/s41467-026-70506-z

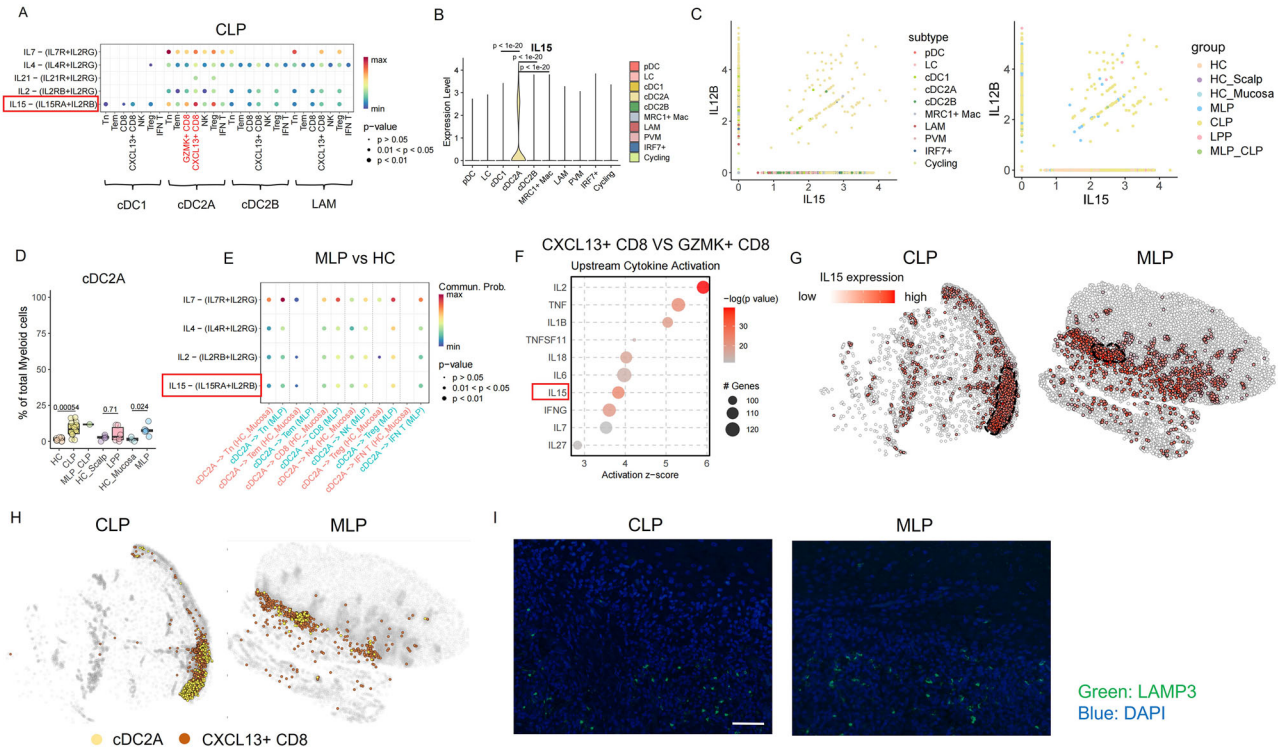

Fig. 6 | Cellular communication analysis reveals cDC2A cells-CXCL13$^+$CD8$^+$ T cells communication through IL-15 signaling. A Heatmap showing statistically significant ligand-receptor pairs mediating cell-cell interactions between myeloid subtypes (ligand) and CXCL13$^+$CD8$^+$ cells (receptor). *P* values were obtained via one-sided permutation tests and are indicated by the circle size. **B** Violin plot showing the expression of *IL15* split by myeloid subtype. The *P* values were calculated by two-sided Wilcoxon test. **C** Scatter plot showing co-expression of *IL15* and *IL12B*. The color represents the identified subtype (left) and disease groups (right). **D** Boxplots showing proportion of cDC2A out of total myeloid cells. HC ($n = 9$), CLP (n = 15), MLP_CLP ($n = 1$), HC_Scalp ($n = 5$), LPP ($n = 6$), HC_Mucosa ($n = 4$), and MLP ($n = 6$). Box plots show the median (center line), interquartile range (box), and 1.5× interquartile range (whiskers). The *P* values were calculated by two-sided Wilcoxon test. **E** Ligand-receptor interaction probabilities of IL-2 signaling between cDC2A (ligand) and T cell subtypes (receptor) in MLP lesions. *P* values were obtained via one-sided permutation tests and are indicated by the circle size. **F** Dot plot showing the top 10 cytokine upstream regulators for differentially expressed genes comparing CXCL13$^+$CD8$^+$ to GZMK$^+$CD8$^+$ cells. Upstream cytokine activation analysis was performed using Ingenuity Pathway Analysis (IPA). The significance of enrichment for each upstream cytokine was assessed using Fisher's exact test. **G** Spatial expression levels of *IL15* in CLP and MLP lesions. **H** Representative images of spatial distribution of CXCL13$^+$CD8$^+$ cells and cDC2A in CLP (left) and MLP (right) lesions. (I) Immunofluorescence showing the expression of LAMP3 in LP lesions. Images shown are representative of $N = 3$. Scale bar = 100 μm. Source data are provided as a Source Data file.

To figure out the critical cytokines regulating the CXCL13$^+$CD8$^+$ cells development, we then used ingenuity pathway analysis (IPA) to identify the top cytokines predicted to serve as upstream regulators for the genes induced in CXCL13$^+$CD8$^+$ cells compared with GZMK$^+$CD8$^+$ cells, identifying IL-15 as one of the top ten upstream regulators of CXCL13$^+$CD8$^+$ enriched transcripts (Fig. 6F). Strikingly, spatial transcriptomics analyses revealed that the expression of *IL15* was perfectly localized with the T cell infiltration area in the CLP and MLP lesions (Fig. 6G). In addition, immunofluorescence staining of LAMP3, a marker of cDC2A cells, revealed a more prominent presence of cDC2A cells in CLP and MLP lesions (Fig. 6I). Taken together, these findings suggest that the development of CXCL13$^+$CD8$^+$ T cells in CLP and MLP is strongly dependent on IL-15 signaling from cDC2A.

Functionally diverse FB subtypes likely drive LP inflammation and fibrosis

While fibrosis is a hallmark of chronic LP, particularly in fibrosing alopecia observed in LPP[21,22], fibroblasts (FBs) have not been comprehensively investigated, especially in the context of distinct LP subtypes. Therefore, we sought to further characterize the phenotypic and functional differences of FBs across the various clinical subtype of LP. We annotated 10 FB subtypes (Supplementary Fig. 7A, B), among which *CCL19*$^+$ FBs and *SFRP2*$^+$ FBs were mainly derived from CLP lesions, while *PTGDS*$^+$ FBs were mainly derived from LPP lesions (Supplementary Fig. 7C). PTGDS was previously considered to be a potential diagnostic marker in oral lichen planus[23]. Enrichment analysis of biological processes associated with the *SFRP2*$^+$ and *CCL19*$^+$ FB subtypes revealed their common involvement in collagen fibril organization and extracellular matrix organization (Supplementary Fig. 7D), with the prominent collagen genes expression identified in these two subtypes (Supplementary Fig. 7E). Furthermore, *SFRP2*$^+$ FBs exhibited high expression of myofibroblast-associated genes, such as *POSTN* and *PRSS23* (Supplementary Fig. 7F), whereas *CCL19*$^+$ FBs expressed a panel of pro-inflammatory cytokines, including *CCL2*, *IL32*, *CCL19*, and *CXCL9* (Supplementary Fig. 7H). Not surprisingly, *SFRP2*$^+$ FBs ranked the highest myogenesis hallmark score (Supplementary Fig. 7G). Taken together, these findings reveal a functional heterogeneity among fibroblasts in CLP lesions, comprising both extracellular matrix components producing *SFRP2*$^+$ FBs and cytokine-enriched, pro-inflammatory *CCL19*$^+$ FBs.

B cells promote an inflammatory response in MLP lesions

For B and plasma cells, we obtained three main subtypes: Effector B cells, Plasma B cells and Germinal center B cells (GC B) (Supplementary Fig. 8A, B). Due to the distinct separation of effector B cells and plasma cells between MLP and healthy mucosa revealed by uniform manifold approximation and projection (UMAP) (Supplementary Fig. 8C), we next sought to identify key differences in their gene expression profiles, which may reflect divergent functional states. Notably, both effector B cells and plasma cells in MLP lesions exhibited upregulated

expression of genes associated with antiviral responses, suggesting an activated immune state in the MLP B cell compartments (Supplementary Fig. 8D). In contrast, their counterparts in CLP lesions displayed a comparatively quiescent transcriptional profile for immune response.

Targeting 4-1BB protects keratinocytes from cytotoxic responses

Following the confirmation of CXCL13$^+$CD8$^+$ cell presence in LP lesions, we next sought to elucidate the developmental origin of this population. Given that previous studies in cancer have identified GZMK$^+$CD8$^+$ T cells as undifferentiated pre-effector cells and CXCL13$^+$CD8$^+$ T cells as a more differentiated stage[15,24], we hypothesized that GZMK$^+$CD8$^+$ cells may give rise to CXCL13$^+$CD8$^+$ cells development in LP pathogenesis. Indeed, CytoTRACE analysis suggested that GZMK$^+$CD8$^+$ cells represented a less differentiated cell population and CXCL13$^+$CD8$^+$ cells were a more differentiated cell population[25] (Fig. 7A, B), validating a potential development trajectory from GZMK$^+$CD8$^+$ to CXCL13$^+$CD8$^+$ cells. Intriguingly, pseudotime trajectory analysis using Monocle revealed a progressive increase in cytotoxic features along the differentiation path (Fig. 7C), particularly marked by the upregulation of *GZMB*, *TNFRSF9*, and *IFNG* in CXCL13$^+$CD8$^+$ cells, and gradual downregulation of early activation genes (Fig. 7D). Consistently, the previously identified T cells infiltration regions in LP lesions showed strong spatial co-localization with the expression of cytotoxicity-related genes, including *CXCL13*, *IFNG*, *TNFRSF9* (Fig. 7E), which indicated a significantly cytotoxic response inside CLP and MLP lesions, caused by CXCL13$^+$CD8$^+$ cells.

Notably, *TNFRSF9*, also known as 4-1BB, is a costimulatory member of the tumor necrosis factor receptor superfamily, mainly expressed by activated T cells[26]. Interestingly, IL-15 signaling has been shown to drive the expression of 4-1BB in effector CD8$^+$ T cells[27], suggesting a potential interaction between cDC2A-derived IL-15 and the upregulation of 4-1BB on CD8$^+$ T cells within LP lesions. Furthermore, previous studies identified 4-1BB and its natural ligand 4-1BBL (*TNFSF9*) as a critical regulator of T cell expansion and activation that holds potential for anti-tumor applications[28,29]. To further validate the spatial distribution and existence of 4-1BB$^+$CD8$^+$ cells in LP lesions at the protein level, we performed spatial proteomics on CLP and MLP samples. Notably, the infiltration of 4-1BB$^+$GZMB$^+$CD8$^+$ T cells was observed specifically in CLP lesions (Fig. 7F), with relatively less infiltration in MLP lesions (Supplementary Fig. 9D). To further substantiate the involvement of 4-1BBL (*TNFSF9*) in disease pathogenesis, we interrogated our scRNA-seq dataset and found that *TNFSF9* was prominently expressed by myeloid cells (cDC2A), fibroblasts, and epithelial cells (Supplementary Figs. 9A and 10A). This expression pattern coincided with the spatial aggregation of fibroblasts, T cells, and myeloid cells in the above-mentioned T cell infiltration region (Supplementary Fig. 9B). More importantly, *TNFSF9* expression was enriched in this aggregating area (Supplementary Fig. 9C), supporting the potential for localized 4-1BB-4-1BBL signaling within the inflammatory niche.

Given the importance of 4-1BB in regulating immune responses, particularly in mediating keratinocyte-T cell interactions through the 4-1BBL/4-1BB axis[30], we hypothesized that therapeutic targeting of the 4-1BB pathway may offer a promising strategy for treating LP, particularly in patients with CLP. To further evaluate the therapeutic potential of 4-1BB blockade in LP, we employed an established in vitro co-culture model incorporating keratinocytes and peripheral blood mononuclear cells (PBMCs) derived from healthy donors[7]. To recapitulate the heightened cytotoxic environment observed in LP lesions, keratinocytes were pre-treated with IFN-γ and co-cultured with CD3/CD28-activated PBMCs at a 10:1 ratio (PBMCs:keratinocytes), according to our previous experience[7]. We first observed an upregulation of *TNFSF9* in keratinocytes and *TNFRSF9* in CD8$^+$ T cells, confirming the activation of the 4-1BBL/4-1BB axis in this co-culture system (Supplementary Fig. 9E). In addition, we detected increased *IFNG* expression (a key cytotoxic mediator) in CD8$^+$ T cells after co-culture with keratinocytes (Supplementary Fig. 9F). Remarkably, Annexin V-propidium iodide (PI) flow cytometry revealed a significant reduction in keratinocyte cell death upon treatment with anti-TNFRSF9, as indicated by decreased Annexin V$^+$ staining, compared with untreated controls (Fig. 7G and Supplementary Fig. 9G). To further strengthen the translational relevance of 4-1BB blockade in human LP, we reanalyzed previously published scRNA-seq data from cutaneous LP patients who received oral baricitinib (Janus kinase 1/2 inhibitor, JAKi) treatment[12], and observed a marked reduction in TNFRSF9 expression, particularly within CXCL13$^+$CD8$^+$ T cells (Supplementary Fig. 11A, B). Together, these data suggest that drugs targeting 4-1BB signaling should be assessed for the future treatment of CLP and MLP.

Discussion

Here, through an integrative approach combining scRNA-seq, spatial transcriptomics, spatial proteomics, and functional validation experiments, we provide a map of the cellular composition and spatial architecture of LP pathogenesis with unprecedented resolution. To date, the level of published study of LP has been largely limited to immunohistochemistry and global gene analysis[10,31], possibly leading to a biased understanding of its pathogenesis, such as with the previously proposed involvement of IL-17 signaling in LP[10,32]. However, through multi-omics integration analyses, our study provides compelling evidence that LP lesions are primarily driven by cytotoxic responses centered around IFN-γ. Although a previous study has performed small-sample scRNA-seq analysis on oral lichen planus samples from MLP patients[33], the absence of healthy mucosal controls and the restriction to oral lesions limited their ability to provide a comprehensive understanding of LP pathogenesis, thereby hindering the development of broadly applicable therapies across distinct clinical subtypes. By contrast, our study demonstrates how lesional microenvironment is orchestrated through cellular crosstalk between immune cells and epithelial cells across the three distinct clinical subtypes. More specifically, we establish that two critical immune subtypes enriched in CLP and MLP lesions; CXCL13$^+$CD8$^+$ cells and cDC2A cells play a major role in shaping and perpetuating the cytotoxic response in epithelial cells through IFN-γ and TNF. As a result, keratinocytes are subjected to IFN-γ stimulation, leading to the upregulation of Th1-associated mediators such as CXCL9 and CXCL10 [34], particularly in CLP lesions. Our data further indicate that 4-1BB may serve as a promising therapeutic target for the treatment of LP.

While it has been suggested that CD8$^+$ T cells are central disease mediators, with cytotoxicity mediated through IFN-γ priming of KCs through MHC class I induction and cell death[7], the precise cellular heterogeneity in CD8$^+$ T cells is unclear. Consistent with our previous finding[12], CXCL13$^+$CD8$^+$ T cells are the major source of IFN-γ and GZMB in LP. Remarkably, CXCL13$^+$CD8$^+$ T cells may serve as a prognostic biomarker, as their abundance decreases following Baricitinib (a Janus kinase 1/2 inhibitor) treatment in LP patients[12]. This population, previously observed in various tumors, such as breast cancer[35], uterine cancer[36] and melanoma[37], has been associated with enhanced immunotherapy responses and improved overall survival, highlighting a broader link between CXCL13 expression and anti-tumor immunity. However, the involvement of CXCL13$^+$CD8$^+$ T cells in skin inflammation had not been fully reported and the mechanisms underlying their formation in the skin remain poorly understood. Here, we show that cDC2A cells in LP lesions are characterized by high IL-15 expression, which serves as a dominant activating signal for CXCL13$^+$CD8$^+$ T cells. IL15 is a pleiotropic cytokine known to enhance CD8$^+$ T-related immune responses to tumor cells[38]. Furthermore, studies on vitiligo, an autoimmune skin disease mediated by CD8$^+$ T cells that target melanocytes, have demonstrated that IL-15 blockades impaired

https://doi.org/10.1038/s41467-026-70506-z

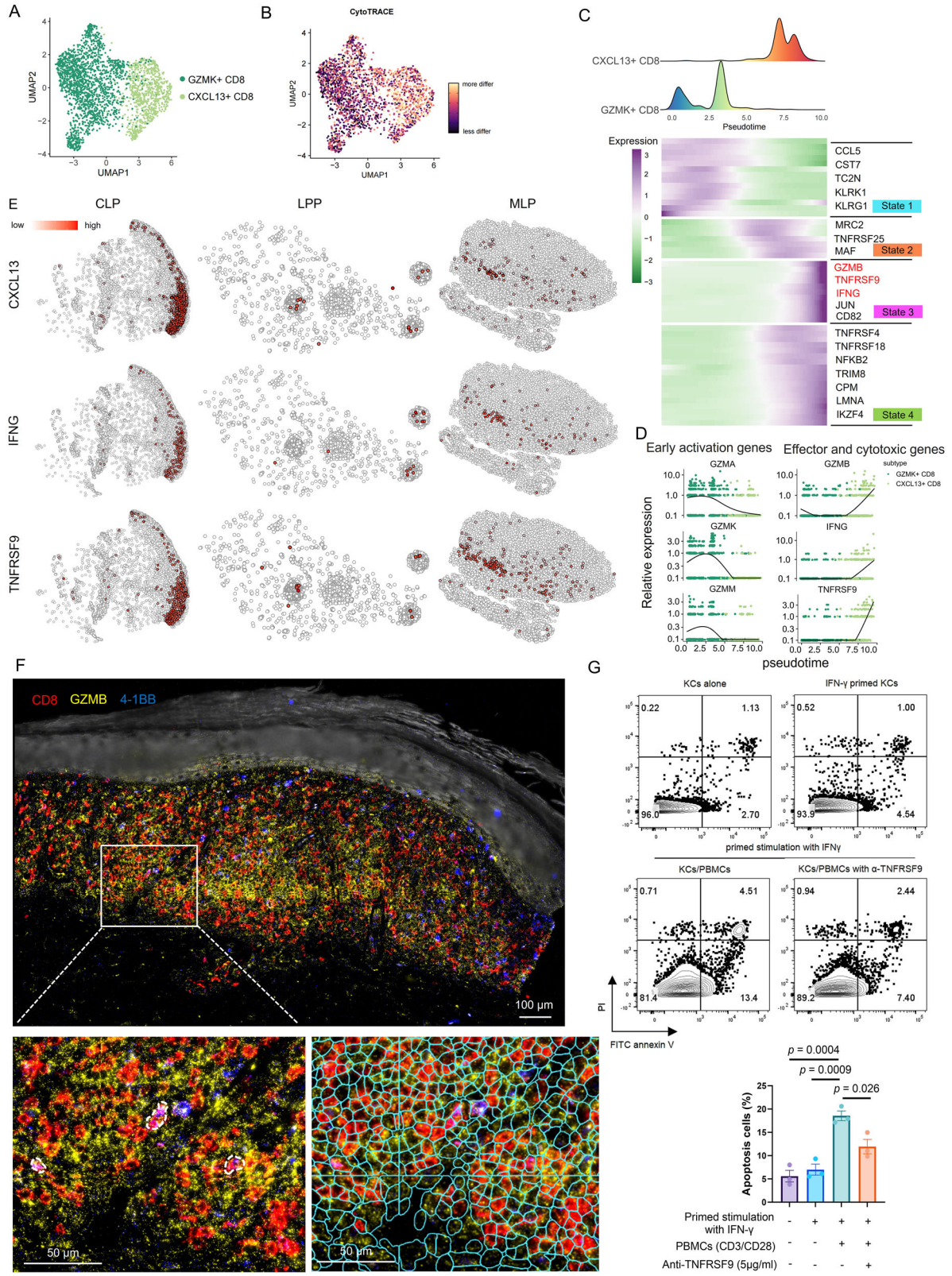

Fig. 7 | Targeting 4-1BB protects keratinocytes from cytotoxic responses. **A** UMAP plot showing $CD8^+$ cells colored by subtypes. **B** UMAP plot showing the CytoTRACE score in two $CD8^+$ subtypes. **C** Heatmap of ordered pseudotime analysis based on monocle showing variable genes along the pseudotime of the $CD8^+$ subtypes. **D** Scatter plot showing expression of transcriptional signature plotted over pseudotime. **E** Spatial expression levels of *CXCL13*, *IFNG*, and *TNFRSF9* in CLP, LPP, and MLP lesions. **F** Representative image of a CLP skin section showing the localization of $CD8^+GZMB^+4\text{-}1BB^+$ cells generated by AtoMx Spatial Informatics Platform. Scale bar, 50 or 100 μm. **G** Keratinocytes (N/TERT) were cocultured with CD3/CD28 microbead-activated PBMCs from healthy donor, and cell death was evaluated by annexin V-PI staining ($n = 3$ biologically independent samples). The representative flow cytometry data (up) and summary (bottom) are shown. Data are presented as the means ± SEM of measurements obtained in triplicate experiments; one-way ANOVA. Source data are provided as a Source Data file.

memory CD8⁺ T cells formation and reverses disease progression[39]. In line with this, our analyses identify IL-15 as one of the key regulators driving the upregulated gene phenotype of CXCL13⁺CD8⁺ T cells. Taken together, our findings build upon existing evidence and corroborate that the development of CXCL13⁺CD8⁺ T cells is dependent on IL-15 signaling from cDC2A cells in the pathogenesis of LP.

Notably, our study delineates the transitional trajectory from GZMK⁺CD8⁺ to CXCL13⁺CD8⁺ T cells, establishing the developmental origin of the CXCL13⁺CD8⁺ T cell population in LP. This trajectory is characterized by a progressive acquisition of cytotoxic features, including the upregulation of *GZMB* and *IFNG* (Fig. 7C, D). GZMK⁺CD8⁺ cells, as an early differentiated subset with relatively limited cytotoxic function, have been widely recognized in several cancer and autoimmune studies[14,24,40,41]. In particular, a recent study in breast cancer identified a CD8⁺ T cell differentiation trajectory, in which peak expression of *GZMA*, *GZMK*, and *GZMM* occurs early, whereas effector genes (e.g., *IFNG*), cytotoxic genes (e.g., *GZMB*), and early exhaustion markers (e.g., *PDCD1*) are upregulated during later stages of differentiation[15], consistent with our observations on CD8⁺ T cells trajectory in LP lesions (Fig. 7D). Furthermore, our analysis of T cell subtype distributions reveals that GZMK⁺CD8⁺ cells are abundant in healthy skin and mucosa but reduced in LP lesions (Supplementary Fig. 4A), whereas CXCL13⁺CD8⁺ T cells are enriched in inflamed lesions. Taken together, these findings suggest that the loss of GZMK⁺CD8⁺ cells and the expansion of CXCL13⁺CD8⁺ cells contribute to the pathogenic cytotoxic landscape in LP, explaining the higher cytotoxic activation in LP lesions.

In addition, our study reveals a previously unrecognized key pathogenic component within CD8⁺ T cells, marked by the upregulation of *TNFRSF9* (4-1BB), particularly in the CXCL13⁺CD8⁺ subset. 4-1BB, an inducible co-stimulatory molecule, is expressed on various types of immune cells, including activated T cells[42], and is upregulated following T-cell receptor (TCR)/CD3 activation. 4-1BB signaling preferentially promotes the activation and survival of CD8⁺ T cells via TRAF1/2 to NF-κB and c-Jun[43], and prevents activation-induced cell death (AICD) of CD8⁺ T cells[44], underscoring its critical role in regulating cytotoxic immune responses. Intriguingly, a previous study demonstrated that keratinocyte-T cell interactions through the 4-1BBL/4-1BB axis can induce cutaneous type-17 inflammation, suggesting a potential broader role for 4-1BB in inflammatory skin diseases[30]. Moreover, to investigate the underlying cause of 4-1BB upregulation in CXCL13⁺CD8⁺ cells, a previous study provided important insights by identifying IL-15 as an essential signal for inducing 4-1BB expression in CD8⁺ effector T cells[27]. This finding aligns well with our previous cellular interaction analysis, which revealed that cDC2A cells promote the activation of CXCL13⁺CD8⁺ T cells via IL-15 signaling. Taken together, our study proposes that IL-15 may serve as a critical upstream regulator of 4-1BB⁺CD8⁺ T cell responses in LP.

Together with our observation of aggregated *TNFRSF9* and *CXCL13* expression in T cell infiltration regions (Fig. 7E), and the presence of *TNFSF9*⁺ fibroblasts, myeloid cells, and epithelial cells in the surrounding microenvironment (Supplementary Fig. 9), it is tempting to speculate that blocking the 4-1BB-4-1BBL axis may represent a promising strategy to modulate CD8⁺ T cell further activation and alleviate the immunopathological manifestations of CLP and MLP. Recent clinical trials have demonstrated the efficacy of anti-4-1BB agonist as a novel therapeutic approach for treating patients with malignancy[45–47]. However, according to our knowledge, the antagonism of this target has not previously been demonstrated in skin inflammation. Given that destruction of basal keratinocytes is due to apoptosis in LP[48], our data corroborate that the blockade of 4-1BB signaling reduces keratinocyte apoptosis and cytotoxic activity, as evidenced by Annexin V-PI flow cytometry. Mechanistically, in our PBMC-keratinocyte co-culture system, 4-1BB blockade likely impedes the interaction between 4-1BB expressed on CD8⁺ T cells and 4-1BBL expressed on myeloid cells, such as dendritic cells, thereby attenuating T cell-mediated cytotoxicity. Of note, due to the limited infiltration of CXCL13⁺CD8⁺ cells and cDC2A cells in LPP (Fig. 4E and Fig. 6D), we anticipate that the anti-4-1BB strategy may be primarily effective in CLP and MLP lesions.

While we employed a sophisticated in vitro model to investigate LP pathogenesis, a key limitation of this study is that the efficacy of the anti-4-1BB antagonist was evaluated in an in vitro system assessing T cell responses against keratinocytes, rather than in actual skin lesions. To address this limitation, we analyzed our previously published scRNA-seq dataset derived from a clinical trial of JAK inhibitor. Notably, we observed a concomitant reduction in TNFRSF9 expression in T cells, accompanied by substantial clinical efficacy, thereby supporting 4-1BB as a promising therapeutic candidate. As such, the pathogenic communication network among cDC2A cells, CXCL13⁺CD8⁺ T cells, and epithelial cells is difficult to fully recapitulate under in vitro conditions. This is largely due to the challenges in inducing both cDC2A cells and CXCL13⁺CD8⁺ T cells in vitro, which also hampers the experimental validation of IL-15 signaling as a potential therapeutic target. Besides, future studies are warranted to assess the therapeutic efficacy of 4-1BB blockade in LP skin lesions and across different clinical subtypes. Furthermore, our study sought to comprehensively interrogate the immune microenvironment and molecular perturbations across the various clinical subtypes of LP. However, compared with CLP and MLP, immune cell infiltration in LPP was sparse and spatially restricted, rendering it less discernible. Notably, LPP lesions exhibited a predominance of lipid-associated macrophages with pro-inflammatory features, while active lymphocyte populations were largely diminished. This immunological landscape may limit the applicability of 4-1BB blockade therapy in LPP patients.

Methods

Human sample acquisition

Sixteen patients with cutaneous lichen planus (CLP) were enrolled in this study, including one individual diagnosed with both CLP and mucosal lichen planus (MLP), from whom a skin biopsy was obtained. Additionally, six patients with lichen planopilaris (LPP) and six patients with MLP were recruited (Supplementary Table 1), along with matched healthy controls: nine healthy skin samples, five healthy scalp samples, and four healthy mucosal samples. All participants provided written informed consent, and the study was approved by the Institutional Review Board (IRB) of the University of Michigan. Skin biopsies (6-mm punch) were obtained from lesional or healthy regions, and all procedures were conducted in accordance with the principles outlined in the Declaration of Helsinki.

Single-cell RNA-seq library preparation, sequencing, and alignment

Tissue dissociation and library construction were performed by the University of Michigan Advanced Genomics Core using the 10X Genomics Chromium platform, following the manufacturer's protocols. Briefly, three 50-µm FFPE tissue scrolls were placed into a GentleMACS C-tube (Miltenyi Biotec) and processed with the GentleMACS Octo Dissociator. The scrolls were deparaffinized, washed, and enzymatically dissociated into a single-cell suspension using Liberase TH. Library preparation was carried out using the 10X Chromium Next GEM chemistry, and sequencing was performed on an Illumina NovaSeq X system to generate 150-bp paired-end reads.

Cell clustering and cell type annotation

Cell clustering analysis was performed using the Seurat R package (v5.0.1) on the combined gene expression matrix[49]. Low-quality cells, defined as those with fewer than 200 detected features or with mitochondrial gene content exceeding 10%, were excluded. Gene expression levels were normalized using the NormalizeData

function with default parameters. Highly variable genes were identified via the FindVariableFeatures function, followed by data scaling and centering using ScaleData. Principal component analysis was performed on the highly variable genes, and the top 20 principal components were used in the RunHarmony function from the Harmony package (v0.1.1) to remove potential batch effect among samples processed in different libraries[50]. UMAP dimensional reduction was performed using the RunUMAP function. Cell clusters were determined using the FindNeighbors and FindClusters functions with a resolution of 0.5. Cluster-specific marker genes were identified using the FindAllMarkers function, and cell type annotations were assigned by mapping the cluster markers to established canonical cell type signature genes.

Cell type sub-clustering

Sub-clustering was conducted for the most abundant cell types using the same functions described previously. Sub-clusters that were defined dominantly by mitochondrial gene expression, indicating low quality, were removed from further analysis. Subtypes were annotated by cross-referencing the marker genes of sub-clusters with canonical subtype signature genes. To investigate the characteristic differences among cell clusters, the "FindAllMarkers" function in the Seurat package was applied to identify differentially expressed genes (DEGs) in individual clusters using the Wilcoxon rank-sum test. Genes with adjusted P value < 0.05 and avg_log2FC > 1 were considered upregulated, while genes with adjusted P value < 0.05 and avg_log2FC < −1 were classified as downregulated. Gene Ontology and KEGG pathway enrichment analyses were conducted using the clusterProfiler package (v4.8.3).

Integration with KC cytokine signatures

We used RNA-seq-based KC cytokine response signatures for the following cytokines: IFNα (10 ng/mL), IFNγ (10 ng/mL), IL-17A (10 ng/mL), TNF (10 ng/mL), or IL-1β (10 ng/mL)[51]. Briefly, primary human KCs from 50 donors were treated with a panel of cytokines as above for 8 h and harvested for RNA isolation. Bulk RNA-seq was performed on the Illumina NovaSeq 6000 sequencer with the assistance of the University of Michigan Advanced Genomics Core. For each stimulation condition versus unstimulated controls, differential expression analysis was performed using DESeq2[52]. DEGs (two-fold increase; false discovery rate, <0.05) were used to construct response signatures for each cytokine.

Calculation of enrichment score

To describe the functional features of cell subtypes, the gene sets of 50 hallmarks were obtained from the MSigDB database[53]. The score of above-mentioned pathways was calculated using gsva function in GSVA package (V1.48.3)[54], and AUCell_calcAUC function in AUCell package (V1.22.0)[55].

Cell–cell interaction inference

The ligand-receptor (LR) interaction analysis was first performed through CellChat (v1.6.1)[19]. The primary analysis focused on interactions between myeloid cell subtypes and T cell subtypes. A separate run was performed for each sample group and the number of significant interactions was calculated for each cell type pair. In addition, the cellular interaction was further confirmed by NicheNet (v2.0.6) package to analyze the different LR pairs between different LP subtypes and healthy control group[18]. For example, in the Fig. 5F, CXCL13+ CD8+ cells were defined as "sender" cells, and epithelial cells were defined as "receiver" cells.

Pseudotime trajectory construction

Pseudotime trajectory analysis was performed using the Monocle package (v2.28.0)[56]. Raw cell counts from the Seurat analysis were normalized using the estimateSizeFactors and estimateDispersions functions with default settings. Genes with an average expression above 0.5 and present in at least 10 cells were retained for further analysis. Variable genes were identified using the FindVariableFeatures function. Cell ordering was determined using the orderCells function, and the trajectory was constructed with the reduceDimension function, both applied with default parameters.

Spatial sequencing library preparation

Formalin-fixed punch biopsies from patients were paraffin-embedded using the Leica ASP 300S (15-min stations) and combined into a single block within a 10 × 22 mm area at the Orthopaedic Research Laboratories (ORL) Histology Core at the University of Michigan. A 5 μm section of the combined tissue block was then mounted onto a Xenium slide (10X Genomics) and processed using a 480-gene custom panel (10X Genomics, design ID G9P69P) on the Xenium Analyzer (10X Genomics) at the University of Michigan Advanced Genomics Core, following the manufacturer's instructions.

Spatial sequencing data analysis

After the Xenium run, H&E staining was performed on the Xenium slide. For quality control of Xenium analysis, the output summary HTML file confirmed that the number of detected transcripts was compatible with that in the reported literature by 10x Genomics[57]. During preprocessing, cells with fewer than 20 counts and negative features (detected in less than 5 cells) were removed from analysis. With the R package Giotto v4.3.0[58], a Giotto object was created based on the flat files, including cell_boundaries.csv.gz, cell_feature_matrix, etc. Information, including the gene expression matrix, cell boundaries, and spatial locations of transcripts for each field of view (FOV), was incorporated into a Giotto object with the Giotto function "createGiottoObject". Cell type annotations were performed using the Giotto function "deconvolution_results", utilizing a reference profile from our single-cell RNA sequencing dataset.

Immunofluorescence staining

Paraffin-embedded tissue sections from punch biopsies of lichen planus patients or healthy controls were incubated at 60 °C for 30 min, followed by deparaffinization and rehydration. Slides were placed in antigen retrieval buffer and heated at 125 °C for 30 s in a pressure cooker water bath. After cooling, slides were blocked using 10% goat serum for 30 min. Overnight incubation was then performed using anti-CD8 (Thermo Fisher Scientific, cat. MA5-13473), anti-CXCL13 (Thermo Fisher Scientific, cat. PA5-28827), anti-KRT5 (Thermo Fisher Scientific, cat. MA5-12596), anti-CXCL9 (R&D Systems, cat. AF392), and anti-LAMP3 (Thermo Fisher Scientific, cat. PA5-84069) in 4 °C. All primary antibodies mentioned above were diluted 1:100. Images presented are representative of at least three biological replicates.

FFPE tissue preparation for spatial proteomics

Tissue samples were collected immediately after excision, cut into sections no thicker than 4–5 mm, and fixed in 10% neutral-buffered formalin (NBF) at room temperature for 24 h to preserve morphology and prevent autolysis and specimens were processed through a graded ethanol series for dehydration (70% ethanol for 1 h, 95% ethanol for 2 × 1 h, and 100% ethanol for 2 × 1 h) followed by clearing in xylene. Tissues were infiltrated with molten paraffin wax at 58–60 °C for 1 h, with gentle vacuum applied to remove trapped air. Samples were then embedded in metal molds filled with molten paraffin, oriented to facilitate sectioning, and allowed to solidify at room temperature. Paraffin blocks were sectioned into 4–5 μm slices using a rotary microtome. Sections were floated on a 42 °C water bath, mounted onto positively charged glass slides, and dried overnight at 37 °C or for 2 h at 60 °C to ensure adhesion.

CosMx Spatial Molecular Imager (SMI) protein assay

Formalin-fixed paraffin-embedded (FFPE) human tissue sections, 5 μm thick, were mounted on standard glass slides for spatial protein analysis. The tissue sections were deparaffinized and rehydrated, followed by antigen retrieval according to the manufacturer's protocol. Tissue sections were incubated with the CosMx Human Immuno-Oncology Protein Panel that enables high-plex spatial analysis of 64 proteins, and the slides were incubated with the probe mix in a humidified chamber at 4 °C for 16–18 h to ensure optimal binding. Following hybridization, slides were washed to remove unbound probes and reduce background signal. Fluorescent imaging of tissue sections was performed on the CosMx Spatial Molecular Imager, configuration A (30 s) was used for the pre-bleaching profile and configuration A (non-neural human cells) was used for the segmentation profile. Tissue architecture and protein localization were visualized using a combination of DAPI staining for nuclei and fluorescently labeled probes specific to cell types of interest. High-resolution imaging was used to guide the selection of Fields of View (FOVs). FOVs were defined based on histological features, marker expression, or areas of interest.

The CosMx SMI system simultaneously quantified protein expression at subcellular resolution by detecting the oligonucleotide barcodes conjugated to the protein-specific antibodies. Subcellular compartments (e.g., nucleus, cytoplasm, membrane) were segmented using computational algorithms integrated with the CosMx platform, enabling spatially resolved protein quantification within each FOV. Raw protein expression data were processed using the CosMx SMI analysis pipeline. Barcode counts were normalized to internal controls, and protein expression levels were mapped spatially across the tissue. Atomx analysis was integrated to segment cells and visualization of the spatial distribution of the protein panel.

Isolation of PBMCs

Peripheral blood samples from healthy donors were collected in University of Michigan Hospital. The study was approved by the University of Michigan Institutional Review Board (IRB), and all donors provided written informed consent. Peripheral Blood Mononuclear Cells (PBMC) were prepared by centrifugation on a Ficoll gradient using Lymphoprep (COSMO BIO USA, cat. AXS-1114544).

Co-culture model of keratinocytes and PBMCs

Both PBMCs and keratinocytes were cultured in 6 well plate. N/TERTs, an immortalized keratinocytes line[13,59], was used in the co-culture system. PBMCs (2×10^6/ml) were pre-stimulated with CD3/CD28 microbeads (Miltenyi Biotec, cat. 130-091-441) for 72 h in RPMI 1640 medium (Gibco, cat. 11875093) supplemented with 10% fetal bovine serum and 1% penicillin-streptomycin. N/TERT cells (about 1×10^5 per well), which were cultured in Keratinocyte-SFM medium (Thermo Fisher Scientific, cat. 17005-042) supplemented with 30 μg/mL bovine pituitary extract, 0.2 ng/mL epidermal growth factor, and 0.3 mM calcium chloride, were washed and stimulated with 10 ng/mL IFN-γ for the first 24 h, followed by replacing the fresh Keratinocyte-SFM medium. N/TERT cells were then co-cultured with pre-stimulated PBMCs (1×10^6 per well). After co-culture for 72 h, N/TERT cells were then washed with PBS twice and collected for flow cytometry of Annexin V-PI analysis for analyzing cell death. To block the signal of TNFRSF9, blocking antibody targeting TNFRSF9 (1:100, Thermo Fisher, cat. MA5-49969) was employed in the co-culture model for 72 h.

RNA extraction and qRT-PCR

After co-culture, keratinocytes and $CD8^+$ T cells were then harvested for RNA extraction. $CD8^+$ T cells were isolated from suspended PBMCs by negative selection using $CD8^+$ T Cell Isolation Kit (Miltenyi biotec, cat. 130-096-495). RNAs were isolated from cell cultures using RNeasy plus kit (Qiagen, cat. 74136). Reversed transcription was performed using a High-Capacity cDNA Transcription kit (Thermo Fisher Scientific, cat. 4368813). qPCR was performed on a 7900HT Fast Real-time PCR system (Thermo Fisher Scientific) with TaqMan Universal PCR Master Mix (Thermo Fisher Scientific, cat. 4304437) using TaqMan primers (Thermo Fisher Scientific, TNFSF9: Hs00169409_m1; TNFRSF9: Hs00155512_m1; IFNG: Hs00989291_m1). RPLP0 (Thermo Fisher Scientific, Hs99999902_m1) was used as an endogenous control.

Statistical data analysis

The Wilcoxon rank-sum test (two-sided) was employed for scRNA-seq marker gene analyses and differential expression analysis. Enrichment analysis was performed using the hypergeometric test. Group comparisons were conducted using Prism software (GraphPad) with ordinary one-way analysis of variance (ANOVA) for comparisons across different groups. Data are presented as individual data points with means ± SEM. P value of <0.05 was considered statistically significance.

Reporting summary

Further information on research design is available in the Nature Portfolio Reporting Summary linked to this article.

Data availability

The scRNA-seq data generated are available in GEO under accession number GSE317789 (https://www.ncbi.nlm.nih.gov/geo/). The spatial transcriptomics data generated for LP samples are available in Zenodo (Lichen_Planus). The spatial proteomics data generated for LP samples are also available in Zenodo (Lichen_Planus_proteomics). All data are included in the Supplementary Information or available from the authors, as are unique reagents used in this article. The raw numbers for charts and graphs are available in the Source Data file whenever possible. Source data are provided with this paper.

References

1. Boyd, A. S. & Neldner, K. H. Lichen planus. *J. Am. Acad. Dermatol.* **25**, 593–619 (1991).
2. Tziotzios, C. et al. Lichen planus and lichenoid dermatoses: clinical overview and molecular basis. *J. Am. Acad. Dermatol.* **79**, 789–804 (2018).
3. Kang, H., Alzolibani, A. A., Otberg, N. & Shapiro, J. Lichen planopilaris. *Dermatol. Ther.* **21**, 249–256 (2008).
4. Alrashdan, M. S., Cirillo, N. & McCullough, M. Oral lichen planus: a literature review and update. *Arch. Dermatol. Res.* **308**, 539–551 (2016).
5. Zhou, X. J., Sugerman, P. B., Savage, N. W., Walsh, L. J. & Seymour, G. J. Intra-epithelial CD8+ T cells and basement membrane disruption in oral lichen planus. *J. Oral. Pathol. Med.* **31**, 23–27 (2002).
6. Viguier, M. et al. Peripheral and local human papillomavirus 16-specific CD8+ T-cell expansions characterize erosive oral lichen planus. *J. Investig. Dermatol.* **135**, 418–424 (2015).
7. Shao, S. et al. IFN-γ enhances cell-mediated cytotoxicity against keratinocytes via JAK2/STAT1 in lichen planus. *Sci. Transl. Med.* **11**, https://doi.org/10.1126/scitranslmed.aav7561 (2019).
8. Pietschke, K. et al. The inflammation in cutaneous lichen planus is dominated by IFN-ϒ and IL-21-A basis for therapeutic JAK1 inhibition. *Exp. Dermatol.* **30**, 262–270 (2021).
9. Popovska, M. et al. T-cell subpopulations in lesions of oral lichen planus. *Pril. (Makedon. Akademija na Naukite i Umetnostite. Oddelenie za Medicinski Nauk.)* **34**, 143–149 (2013).
10. Mahmoud, S. B., Anwar, M. K., Shaker, O. G. & El Sharkawy, D. A. Possible Relation between Vitamin D and Interleukin-17 in the Pathogenesis of Lichen Planus. *Dermatology* **237**, 896–901 (2021).
11. Wang, H. et al. Role of distinct CD4(+) T helper subset in pathogenesis of oral lichen planus. *J. Oral. Pathol. Med.* **45**, 385–393 (2016).

12. Hwang, A. S. et al. Rapid response of lichen planus to baricitinib associated with suppression of cytotoxic CXCL13+CD8+ T cells. *J. Clin. Investig.* **135**, https://doi.org/10.1172/jci179436 (2024).
13. Ma, F. et al. Single cell and spatial sequencing define processes by which keratinocytes and fibroblasts amplify inflammatory responses in psoriasis. *Nat. Commun.* **14**, 3455 (2023).
14. Jonsson, A. H. et al. Granzyme K(+) CD8 T cells form a core population in inflamed human tissue. *Sci. Transl. Med.* **14**, eabo0686 (2022).
15. Bassez, A. et al. A single-cell map of intratumoral changes during anti-PD1 treatment of patients with breast cancer. *Nat. Med.* **27**, 820–832 (2021).
16. Cheuk, S. et al. CD49a expression defines tissue-resident CD8(+) T cells poised for cytotoxic function in human skin. *Immunity* **46**, 287–300 (2017).
17. Ryan, G. E., Harris, J. E. & Richmond, J. M. Resident memory T cells in autoimmune skin diseases. *Front. Immunol.* **12**, 652191 (2021).
18. Browaeys, R., Saelens, W. & Saeys, Y. NicheNet: modeling intercellular communication by linking ligands to target genes. *Nat. Methods* **17**, 159–162 (2020).
19. Jin, S. et al. Inference and analysis of cell-cell communication using CellChat. *Nat. Commun.* **12**, 1088 (2021).
20. Park, S. L. et al. Divergent molecular networks program functionally distinct CD8(+) skin-resident memory T cells. *Science* **382**, 1073–1079 (2023).
21. Griggs, J., Trüeb, R. M., Gavazzoni Dias, M. F. R., Hordinsky, M. & Tosti, A. Fibrosing alopecia in a pattern distribution. *J. Am. Acad. Dermatol.* **85**, 1557–1564 (2021).
22. Alessandrini, A., Bruni, F., Piraccini, B. M. & Starace, M. Common causes of hair loss - clinical manifestations, trichoscopy and therapy. *J. Eur. Acad. Dermatol. Venereol.* **35**, 629–640 (2021).
23. Lim, D. M. et al. Distinct immunological features compared to Lichen Planus and Oral Lichen Planus. *J. Inflamm. Res.* **18**, 4037–4056 (2025).
24. Schalck, A. et al. Single-cell sequencing reveals trajectory of tumor-infiltrating lymphocyte states in pancreatic cancer. *Cancer Discov.* **12**, 2330–2349 (2022).
25. Gulati, G. S. et al. Single-cell transcriptional diversity is a hallmark of developmental potential. *Science* **367**, 405–411 (2020).
26. Melero, I., Hirschhorn-Cymerman, D., Morales-Kastresana, A., Sanmamed, M. F. & Wolchok, J. D. Agonist antibodies to TNFR molecules that costimulate T and NK cells. *Clin. Cancer Res.* **19**, 1044–1053 (2013).
27. Pulle, G., Vidric, M. & Watts, T. H. IL-15-dependent induction of 4-1BB promotes antigen-independent CD8 memory T cell survival. *J. Immunol.* **176**, 2739–2748 (2006).
28. Pichler, A. C. et al. TCR-independent CD137 (4-1BB) signaling promotes CD8(+)-exhausted T cell proliferation and terminal differentiation. *Immunity* **56**, 1631–1648.e1610 (2023).
29. Shuford, W. W. et al. 4-1BB costimulatory signals preferentially induce CD8+ T cell proliferation and lead to the amplification in vivo of cytotoxic T cell responses. *J. Exp. Med.* **186**, 47–55 (1997).
30. Neuwirth, T. et al. The polyamine-regulating enzyme SSAT1 impairs tissue regulatory T cell function in chronic cutaneous inflammation. *Immunity* **58**, 632–647.e612 (2025).
31. Kurzen, N. et al. Death-associated protein kinase 1 dampens keratinocyte necroptosis and expression of inflammatory genes in Lichen Planus. *J. Investig. Dermatol.* https://doi.org/10.1016/j.jid.2024.11.017 (2024).
32. Javvadi, L. R., Parachuru, V. P., Milne, T. J., Seymour, G. J. & Rich, A. M. Regulatory T-cells and IL17A(+) cells infiltrate oral lichen planus lesions. *Pathology* **48**, 564–573 (2016).
33. Qing, M. et al. CD8(+) tissue-resident memory T cells induce oral lichen planus erosion via cytokine network. *eLife* **12**, https://doi.org/10.7554/eLife.83981 (2023).
34. House, I. G. et al. Macrophage-derived CXCL9 and CXCL10 are required for antitumor immune responses following immune checkpoint blockade. *Clin. Cancer Res.* **26**, 487–504 (2020).
35. Zhang, Y. et al. Single-cell analyses reveal key immune cell subsets associated with response to PD-L1 blockade in triple-negative breast cancer. *Cancer Cell* **39**, 1578–1593.e1578 (2021).
36. Workel, H. H. et al. A transcriptionally distinct CXCL13(+)CD103(+) CD8(+) T-cell population is associated with B-cell recruitment and neoantigen load in human cancer. *Cancer Immunol. Res.* **7**, 784–796 (2019).
37. Veatch, J. R. et al. Neoantigen-specific CD4(+) T cells in human melanoma have diverse differentiation states and correlate with CD8(+) T cell, macrophage, and B cell function. *Cancer Cell* **40**, 393–409.e399 (2022).
38. Ma, R. et al. An oncolytic virus expressing IL15/IL15Rα combined with off-the-shelf EGFR-CAR NK cells targets glioblastoma. *Cancer Res.* **81**, 3635–3648 (2021).
39. Richmond, J. M. et al. Antibody blockade of IL-15 signaling has the potential to durably reverse vitiligo. *Sci. Transl. Med.* **10**, https://doi.org/10.1126/scitranslmed.aam7710 (2018).
40. Lan, F. et al. GZMK-expressing CD8(+) T cells promote recurrent airway inflammatory diseases. *Nature* **638**, 490–498 (2025).
41. Guo, C. L. et al. Granzyme K(+)CD8(+) T cells interact with fibroblasts to promote neutrophilic inflammation in nasal polyps. *Nat. Commun.* **15**, 10413 (2024).
42. Hurtado, J. C., Kim, S. H., Pollok, K. E., Lee, Z. H. & Kwon, B. S. Potential role of 4-1BB in T cell activation. Comparison with the costimulatory molecule CD28. *J. Immunol.* **155**, 3360-3367 (1995).
43. Ward-Kavanagh, L. K., Lin, W. W., Šedý, J. R. & Ware, C. F. The TNF receptor superfamily in co-stimulating and co-inhibitory responses. *Immunity* **44**, 1005–1019 (2016).
44. Wang, C., Lin, G. H., McPherson, A. J. & Watts, T. H. Immune regulation by 4-1BB and 4-1BBL: complexities and challenges. *Immunol. Rev.* **229**, 192–215 (2009).
45. Segal, N. H. et al. Results from an integrated safety analysis of urelumab, an agonist Anti-CD137 monoclonal antibody. *Clin. Cancer Res.* **23**, 1929–1936 (2017).
46. Khushalani, N. I. et al. Final results of urelumab, an anti-CD137 agonist monoclonal antibody, in combination with cetuximab or nivolumab in patients with advanced solid tumors. *J. Immunother. Cancer* **12**, https://doi.org/10.1136/jitc-2023-007364 (2024).
47. Srivastava, R. M. et al. CD137 stimulation enhances cetuximab-induced natural killer: dendritic cell priming of antitumor T-cell immunity in patients with head and neck cancer. *Clin. Cancer Res.* **23**, 707–716 (2017).
48. Brant, J. M., Aguiar, M. C., Grandinetti, H. A., Rodrigues, L. V. & Vasconcelos, A. C. A comparative study of apoptosis in reticular and erosive oral lichen planus. *Braz. Dent. J.* **23**, 564–569 (2012).
49. Butler, A., Hoffman, P., Smibert, P., Papalexi, E. & Satija, R. Integrating single-cell transcriptomic data across different conditions, technologies, and species. *Nat. Biotechnol.* **36**, 411–420 (2018).
50. Korsunsky, I. et al. Fast, sensitive and accurate integration of single-cell data with harmony. *Nat. Methods* **16**, 1289–1296 (2019).
51. Billi, A. C. et al. Nonlesional lupus skin contributes to inflammatory education of myeloid cells and primes for cutaneous inflammation. *Sci. Transl. Med.* **14**, eabn2263 (2022).
52. Love, M. I., Huber, W. & Anders, S. Moderated estimation of fold change and dispersion for RNA-seq data with DESeq2. *Genome Biol.* **15**, 550 (2014).
53. Subramanian, A. et al. Gene set enrichment analysis: a knowledge-based approach for interpreting genome-wide expression profiles. *Proc. Natl. Acad. Sci. USA* **102**, 15545–15550 (2005).
54. Hänzelmann, S., Castelo, R. & Guinney, J. GSVA: gene set variation analysis for microarray and RNA-seq data. *BMC Bioinforma.* **14**, 7 (2013).

55. Corridoni, D. et al. Single-cell atlas of colonic CD8(+) T cells in ulcerative colitis. *Nat. Med.* **26**, 1480–1490 (2020).
56. Trapnell, C. et al. The dynamics and regulators of cell fate decisions are revealed by pseudotemporal ordering of single cells. *Nat. Biotechnol.* **32**, 381–386 (2014).
57. Janesick, A. et al. High resolution mapping of the tumor microenvironment using integrated single-cell, spatial and in situ analysis. *Nat. Commun.* **14**, 8353 (2023).
58. Dries, R. et al. Giotto: a toolbox for integrative analysis and visualization of spatial expression data. *Genome Biol.* **22**, 78 (2021).
59. Dickson, M. A. et al. Human keratinocytes that express hTERT and also bypass a p16(INK4a)-enforced mechanism that limits life span become immortal yet retain normal growth and differentiation characteristics. *Mol. Cell. Bi ology* **20**, 1436–1447 (2000).

Acknowledgements

This work was supported by a non-restricted research grant from the National Institutes of Health (K01AR072129 and R01AR080662 to L.C.T.; 1P30AR075043 to L.C.T., M.T.P., and J.E.G.; UC2 AR081033 to L.C.T. and J.E.G.). This study was supported by non-restrictive funding from Novartis. Sinocare Diabetes Foundation Scholarship for the Michigan-Xiangya MD/PhD Dual Degree Program (awarded to R.J.).

Author contributions

Conceptualization: R.J., J.E.G., F.H.R., and T.A.R.; Methodology: R.J., R.B., X.X., J.K., J.F., H.Z., L.C.T., R.L.M., and J.E.G.; Imaging: X.X. and R.J.; Investigation: R.J., P.W.H., T.D., A.C.B., J.M.K., R.L.M, R.T., J.W., M.A.S., S.B., B.R., G.M.B., F.H.R., T.A.R., A.M., and J.E.G.; Writing: R.J., J.E.G., F.H.R., T.A.R.; Funding Acquisition: L.C.T. and J.E.G. Supervision: J.E.G.

Competing interests

This was an independent, investigator-initiated study supported by Novartis. Novartis was given the opportunity to review the manuscript for medical and scientific accuracy as it relates to Novartis substances, as well as intellectual property considerations. The remaining authors declare no competing interests.

Additional information

Supplementary information The online version contains supplementary material available at https://doi.org/10.1038/s41467-026-70506-z.

Correspondence and requests for materials should be addressed to Johann E. Gudjonsson.

Peer review information *Nature Communications* thanks Yoshihide Asano, Tetsuya Honda, Yu Sawada and the other anonymous reviewer(s) for their contribution to the peer review of this work. A peer review file is available.